Geochemical Perspectives Letters

Consolidating the isotopic trichotomy of planetary materials with new evidence

E. Siciliano Rego, N. Dauphas, T. Hopp

Supplementary Information

The Supplementary Information includes:

- Material and Methods
- Tables S-1 and S-2
- Statistical Approach to Identifying Isotopically Similar Meteorite Groups
- Figures S-1 and S-2
- Supplementary Information References

Material and Methods

A total of 8 samples were measured for their Fe isotopic compositions, including three primitive CC achondrites (NWA 011, NWA 6704/6926/6693, Tafassasset), three carbonaceous chondrites (Coolidge, Renazzo, Bencubbin), and two NC achondrites (Erg Chech 002 and NWA 5400). The CC achondrite samples were selected because their Ti-Cr-O isotopic compositions are similar to CI chondrites (NWA 011, NWA 6926/6704/6693, Tafassasset, Sanborn *et al.*, 2019; Williams *et al.*, 2020) (Fig. 1, see main text). The carbonaceous chondrites and NC achondrites were selected because they represent previously unstudied groups for Fe isotopes (*e.g.,* CL, CB, Erg Chech 002, and NWA 5400), and to assess the robustness of the dataset, for example by measuring Renazzo and verifying whether it exhibits an isotopic composition similar to other CR chondrites. We also analysed the geostandard IF-G, a banded iron formation from Greenland, as it is a well-characterised terrestrial reference material, including for high-precision Fe isotope measurements (Heard *et al*., 2020). This standard shows a small but resolvable μ^{54}Fe offset relative to IRMM-524A due to non-exponential mass fractionation, and our repeated measurements agree with published values (Craddock

and Dauphas, 2011; Heard *et al.*, 2020). All sample processing and analyses were done in the Origins Lab of the University of Chicago. Approximately 40 mg of each whole rock sample was digested using concentrated mixtures of HF-HNO_3 (28 M and 15 M respectively in a 2:1 mixture) at 130 °C on a hotplate for 48 hours. Samples that did not dissolve completely during this step were transferred to Parr bombs and heated at 180 °C in an oven for 72 hours. This step was followed by multiple dissolution steps using aqua regia. Aliquots of the digested samples containing ~1 mg of Fe were processed for chemical purification.

The Fe chemical purification procedure is described by Tang and Dauphas (2012) and Hopp *et al.* (2022a,b). It efficiently separates Fe from matrix and interfering elements. Briefly, samples are loaded in 0.25 mL 10 M HCl onto 10.5 cm-long PFA columns filled with 3 mL pre-cleaned AG1-X8 (200-400 mesh) anion resin. Nickel and other major elements are eluted in 5 mL 10 M HCl, while Cu, Cr and additional contaminants are removed using 30 mL 4 M HCl. Iron is finally eluted and collected using 9 ml 0.4 M HCl. The entire chemical purification procedure is repeated using new resin. After completion of the second purification step, the purified Fe solution was dried down and dissolved in 0.3 M HNO_3 for isotopic analysis.

Iron isotopic measurements were made using a Thermo Scientific Neptune multicollector inductively coupled mass spectrometer (MC-ICP-MS) upgraded to Neptune Plus specifications. Ion beams of $^{54}Fe^+$, $^{56}Fe^+$, $^{57}Fe^+$, and $^{58}Fe^+$ were analysed in static mode on Faraday collectors using a $10^{10}\Omega$ amplifier for $^{56}Fe^+$ and $10^{11}\Omega$ amplifiers for the other Fe isotopes. Isobaric interferences from $^{54}Cr^+$ and $^{58}Ni^+$ were corrected for by monitoring $^{53}Cr^+$ and $^{60}Ni^+$ using 10^{12} Ω amplifiers. Measurements were made on the flat-topped peak shoulders for Fe and peak centers for Cr and Ni, in either high-resolution (HR) mode or medium-resolution (MR) mode to resolve molecular interferences on Fe (Dauphas *et al.*, 2009; Weyer and Schwieters, 2003). Platinum skimmer and sample cones were used (Hopp *et al.*, 2022a). A cyclonic glass spray chamber was used along with an ESI PFA nebulizer to inject the purified Fe solutions (10 µg/g in 0.3 M HNO_3) into the MC-ICP-MS. Each measurement consisted of 50 cycles with an integration time of 8.369 s. Iron isotopic data were bracketed and expressed relative to IRMM-524a, which has an identical isotopic composition to IRMM-014 (Craddock and Dauphas, 2011). The reported isotopic compositions (Table S-1) represent the average of 12 to 15 sample-standard brackets and are expressed in δ-notation,

$$\delta^i Fe\ (‰) = [\ (^iFe/^{54}Fe)_{sample} / (^iFe/^{54}Fe)_{IRMM\text{-}524a} - 1] \times 10^3 \quad \text{.(Eq. S-1)}$$

Iron isotopic anomalies were calculated by correcting for instrumental and natural mass fractionation using the exponential law (Dauphas and Schauble, 2016), and internal normalization to $^{57}Fe/^{56}Fe$=0.023095, the certified ratio of IRMM-014. Isotopic anomalies are reported in the µ-notation,

$$\mu^{i}Fe = [\ (^{i}Fe/^{56}Fe)_{(57/56),sample} / (^{i}Fe/^{56}Fe)_{(57/56),IRMM\text{-}524a} - 1] \times 10^{6}\ ,\quad \text{(Eq. S-2)}$$

where the (57/56) subscript indicates the ratio used for internal normalisation. Uncertainties are based on repeat measurements using Student's t-value for a two-sided 95% confidence interval (95 % c.i.).

Supplementary Tables

Table S-1 Iron isotopic compositions of primitive CC achondrites, carbonaceous chondrites, non-carbonaceous achondrites and IF-G geostandard.

Sample	Group	N	$\mu^{54}Fe$ (7/6)	±	$\mu^{58}Fe$ (7/6)	±	$\delta^{56}Fe$	±	$\delta^{57}Fe$	±
NWA 6704	CC Achondrite	14	36	11	4	10	0.01	0.02	0.03	0.03
NWA 011	CC Achondrite	12	21	5	14	9	0.03	0.03	0.05	0.03
Tafassasset	CC Achondrite	15	33	6	6	12	-0.06	0.02	-0.07	0.03
Coolidge	CL	15	20	8	12	12	-0.04	0.02	-0.06	0.03
Bencubbin	CB	15	36	6	15	10	-0.11	0.02	-0.15	0.03
Renazzo	CR	15	33	8	-	-	0.01	0.02	0.03	0.03
Erg Chech 002	NC achondrite	15	10	6	-	-	0.07	0.02	0.11	0.03
NWA 5400	Achondrite ung.	13	9	8	1	11	-0.02	0.03	-0.03	0.03
IF-G A	Geostandard	8	-11	6	-9	15	0.61	0.02	0.91	0.03
IF-G B	Geostandard	10	-15	9	-10	9	0.65	0.02	0.96	0.03
IF-G (literature)•	Geostandard	24	-16	9			0.61	0.01	0.88	0.02

- $\mu^{58}Fe$ data are not reported for Renazzo and Erg Chech 002 due to temporary instrumental instability during those specific measurements resulting in very large error bars.
- IF-G values were taken from the literature (Heard *et al.,* 2020), which reported small offset in $\mu^{54}Fe$ relative to IRMM 524A attributed to non-exponential mass fractionation effects.

Table S-2 Compilation of isotopic anomalies in meteorites and planetary materials (after Hopp *et al.*, 2022b; Yokoyama *et al.*, 2022; Rüfenacht *et al.*, 2023;; Dauphas *et al.*, 2024)

	$\mu^{54}Fe$	±	$\mu^{50}Ti$	±	$\mu^{54}Cr$	±
CI	0.3	1.6	190	7	147.4	9.2
Ryugu	1	4	183	27	127	18
CM	22.8	2.7	293	11	97.7	5.9
CO	16.3	4.5	353	50	84	13
CV	26.9	3.6	344	14	91.2	3.1
CK	27	4.5	360	51	51.6	6.2
CR	32.4	4.6	241	25	128.4	6.1
CH	15.5	6.6	212	34	149.1	4.7
CB	36.2	6.1	204	7	128.2	4.6
CL	20	8	259	14	73.5	6.1

H	11.8	1.9	-63	13	-38.2	1.6
L	10.6	4.7	-63	2	-39	7
LL	12.9	4.0	-66	4	-42.4	5.1
R	9.3	3.6			-2.5	7.3
EH	5.7	2	-11.6	3.2	3.7	4.8
EL	6.7	1.4	-28	5	3.8	5.4
K					-44	4
Acapulcoite			-131	3.2	-73.7	4.9
Lodranite			-168	31		
Brachinite			-138	13	-45	6.4
Winonaite						
NWA5363/5400	9	8	-101.5	10	-37	13
Angrite			-114.7	2.2	-43	5.3
Aubrite			-5.4	3.9	5	4.5
HED	12	2.5	-123	4	-67.3	6.8
Ureilite	15.5	1.5	-197	14	-87.5	2.7
Moon			-3	4	9	8
Mesosiderite			-126	9.5	-69.8	6
MG pal			-137	8	-39	46
ESPAL					71	18
IAB Complex (IAB+IIICD)	-1	3.9				
IC	12.9	5				
IIAB	20.6	5.5			-82.4	7.8
IIC	35.1	3.7				
IID	24.4	4.9				
IIE					-59	13
IIF						
IIG						
IIIAB	9.8	3.5			-81.2	4.5
IIIE						
IIIF	27	7				
IVA	9	3.9			-47.3	5.6
IVB	28.6	2.2				

Statistical Approach to Identifying Isotopically Similar Meteorite Groups

This section provides a detailed description of the statistical framework used to evaluate isotopic similarities among meteorite groups. We employed hierarchical cluster analysis (HCA) on Z-score normalized isotopic compositions and selected the optimal number of clusters using the Elbow method. Monte Carlo (MC) simulations were used to assess the robustness of our findings under analytical uncertainty.

Z-Score Normalization

All isotopic data were first normalized using Z-score transformation to place variables with different units and variances on a common scale. For each isotopic system (e.g., $\mu^{54}Fe$, $\mu^{50}Ti$, $\mu^{54}Cr$), the Z-score of a given sample was calculated as:

$$Z = (x - m) / \sigma$$

where x is the measured value, m is the mean of the dataset for that isotope, and σ is the standard deviation of the dataset for that isotope system. This normalization was applied independently to each isotope system. Analytical uncertainties were also propagated into Z-space by dividing the error for each group or sample by the same population standard deviation used for normalization.

Hierarchical Cluster Analysis (HCA)

Hierarchical Cluster Analysis (HCA) is a statistical method widely used in multivariate data analysis to identify patterns and natural groupings within complex datasets. This method provides an objective, statistically based grouping of samples avoiding subjective or pre-assumed classifications. In our case, we rely on isotopic anomalies of different elements (*e.g.,* Fe, Ti, Cr) to access statistically defined groups. In order to group samples based on isotopic similarity, we applied HCA using Ward's method as the linkage criterion. Several linkage methods can be used within hierarchical cluster analysis (HCA), including single linkage (based on the closest pair of points between clusters), complete linkage (based on the farthest pair), and average linkage (based on the average distance between all points). In contrast, Ward's method merges clusters in a way that minimises the total within-cluster variance, resulting in clusters that are more internally consistent. This agglomerative algorithm begins by treating each sample as its own cluster and then merges clusters iteratively to minimize the total within-cluster variance. The distances between samples were computed in Euclidean space based on the normalized Z-scores. Although HCA produces a full hierarchy of potential groupings, the final number of clusters is determined afterward. In the following section, we describe how the Elbow method was used to determine the optimal number of clusters.

Elbow Method

To determine the most appropriate number of clusters for HCA, we used the Elbow Method. This involves calculating the within-cluster sum of squares (WCSS) for a range of cluster numbers (typically from 1 to 10). WCSS measures the compactness of clusters by summing the squared Euclidean distances between each data point and the mean of its assigned cluster. As the number of clusters increases, WCSS naturally decreases because each cluster contains fewer points with less internal variability. However, beyond a certain point, adding more clusters leads to only marginal reductions in within-cluster variance. This inflection point, where the rate of decrease sharply levels off, is referred to as the "elbow." In our dataset, this elbow consistently appeared at k = 3, indicating three statistically coherent clusters. This finding was further validated through Monte Carlo simulations that aimed at examining the influence of analytical uncertainties (see below and Fig. S-1).

Monte Carlo Simulations

In order to evaluate the impact of analytical uncertainty on our clustering results, we implemented a Monte Carlo Simulation (MCS) approach using 500 iterations. In each iteration, Z-scores for Fe, Cr, and Ti were randomly perturbed within their reported uncertainties. Hierarchical clustering was then performed using Ward's method on the perturbed dataset. First, we computed the within-cluster sum of squares (WCSS) for cluster numbers ranging from 1 to 10. The average WCSS curve across iterations retained a clear elbow at $k = 3$, supporting the robustness of the original three-cluster interpretation despite uncertainty propagation (Fig. S-1).

Second, to assess the stability of group assignments, we constructed a co-clustering matrix that records how frequently each pair of meteorite groups was assigned to the same cluster across all iterations. This analysis revealed that CI and Ryugu co-clustered with each other in 100 % of simulations, NC samples in 100 %, and CC samples in ~80% of simulations. The slightly lower co-clustering stability within the CC group likely reflects internal substructure among distinct CC subgroups (*e.g.*, CR, CB, Tafassasset), in agreement with previous trace element and isotopic data (Weyrauch *et al.*, 2021; Wölfer *et al.*, 2023), and/or occasional overlaps with a subset of CC meteorites, most notably CH, which co-clustered with CI/Ryugu in ~18 % of simulations (Fig. S-2). This overlap may be attributed to the comparatively low μ^{54}Fe value reported for CH (15.6 ± 6.6 ppm, n=1), based on a single sample (SaU 290, CH3; Schiller *et al.*, 2020). Additional analyses of CH meteorites are needed to determine whether this low value is representative of the group. Overall, this Monte Carlo approach confirms the robustness of the three-cluster structure and highlights the statistical coherence of the CI/Ryugu, CC, and NC groupings under uncertainty.

Supplementary Figures

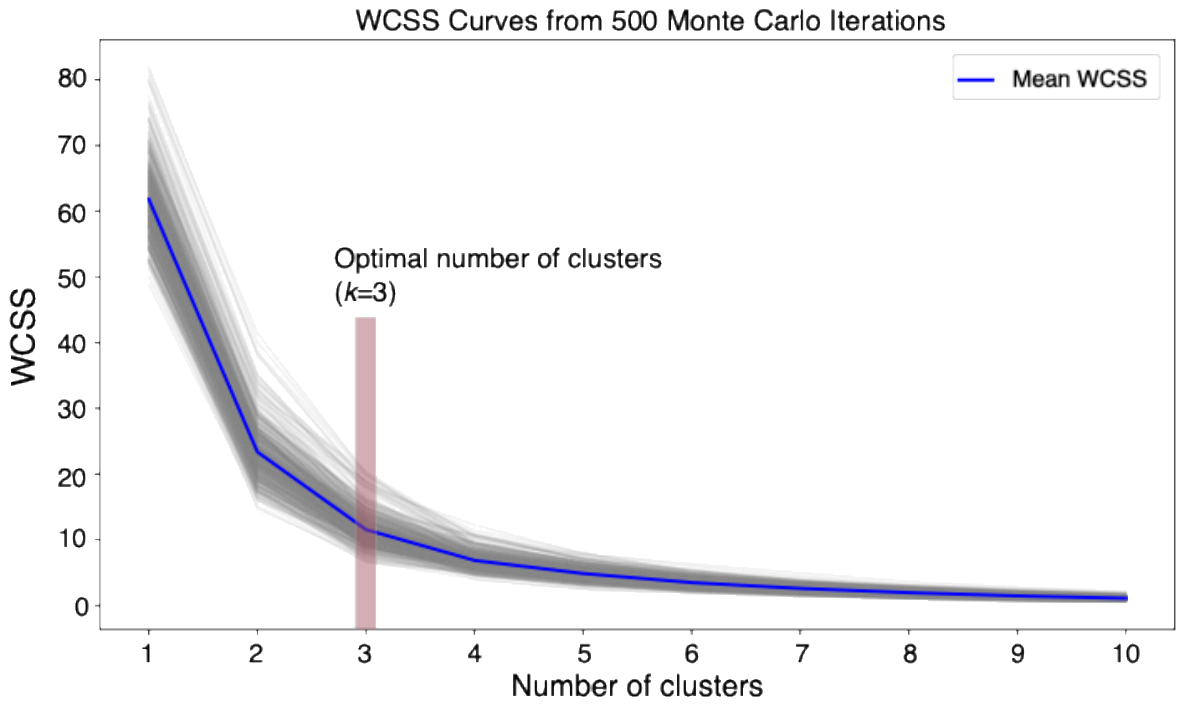

Figure S-1 Monte Carlo simulation of within-cluster sum of squares (WCSS) curves for cluster numbers ranging from 1 to 10. Each grey line represents a WCSS curve from a single iteration (n = 500), in which Fe, Cr, and Ti Z-scores were perturbed based on their analytical uncertainties. The blue line shows the mean WCSS curve across all iterations. The consistent curvature and inflection point around k = 3 across simulations support the selection of three clusters as the optimal solution.

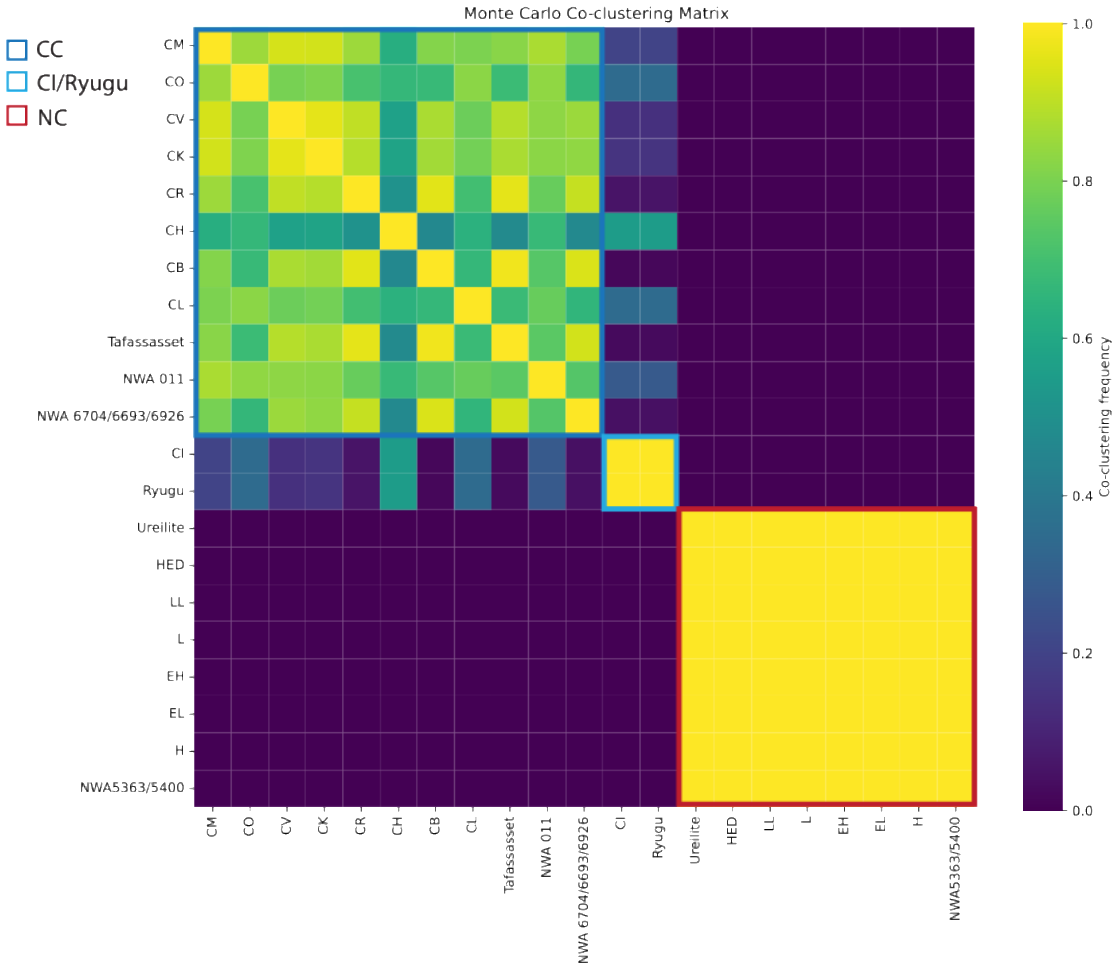

Figure S-2 Co-clustering matrix generated from 500 Monte Carlo simulations in which Fe, Cr, and Ti Z-scores were perturbed based on their reported uncertainties. Hierarchical clustering using Ward's method was applied in each iteration, keeping the number of clusters fixed at three. Each cell shows the frequency (from 0 to 1) with which a given pair of samples was assigned to the same cluster. Brighter values indicate more consistent clustering. The matrix reveals three stable clusters corresponding to NC, CC and, CI/Ryugu as shown highlighted in light red, blue, and light blue, respectively.

Supplementary Information References

Craddock, P.R., Dauphas, N. (2011) Iron Isotopic Compositions of Geological Reference Materials and Chondrites. *Geostandards and Geoanalytical Research* 35, 101–123. https://doi.org/10.1111/j.1751-908X.2010.00085.x

Dauphas, N., Schauble, E.A. (2016) Mass Fractionation Laws, Mass-Independent Effects, and Isotopic Anomalies. *Annual Review of Earth and Planetary Sciences* 44, 709–783. https://doi.org/10.1146/annurev-earth-060115-012157

Dauphas, N., Pourmand, A., Teng, F.Z. (2009) Routine isotopic analysis of iron by HR-MC-ICPMS: How precise and how accurate? *Chemical Geology* 267, 175–184. https://doi.org/10.1016/j.chemgeo.2008.12.011

Dauphas, N., Hopp, T., Nesvorný, D. (2024) Bayesian inference on the isotopic building blocks of Mars and Earth. *Icarus* 408, 115805. https://doi.org/10.1016/j.icarus.2023.115805

Heard, A.W., Dauphas, N., Guilbaud, R., Rouxel, O.J., Butler, I.B., Nie, N.X., Bekker, A. (2020) Triple iron isotope constraints on the role of ocean iron sinks in early atmospheric oxygenation. *Science* 370, 1–5. https://doi.org/10.1126/science.aaz8821

Hopp, T., Dauphas, N., Spitzer, F., Burkhardt, C., Kleine, T. (2022a) Earth's accretion inferred from iron isotopic anomalies of supernova nuclear statistical equilibrium origin. *Earth and Planetary Science Letters* 577, 117245. https://doi.org/10.1016/j.epsl.2021.117245

Hopp, T., Dauphas, N., Abe, Y., Aléon, J., Alexander, C.M.O'D *et al.* (2022b) Ryugu's nucleosynthetic heritage from the outskirts of the Solar System. *Science Advances* 8, 1–10. https://doi.org/10.1126/sciadv.add8141

Rüfenacht, M., Morino, P., Lai, Y.J., Fehr, M.A., Haba, M.K., Schönbächler, M. (2023) Genetic relationships of solar system bodies based on their nucleosynthetic Ti isotope compositions and sub-structures of the solar protoplanetary disk. *Geochimica et Cosmochimica Acta* 355, 110–125. https://doi.org/10.1016/j.gca.2023.06.005

Sanborn, M.E., Wimpenny, J., Williams, C.D., Yamakawa, A., Amelin, Y., Irving, A.J., Yin, Q.Z. (2019) Carbonaceous achondrites Northwest Africa 6704/6693: Milestones for early Solar System chronology and genealogy. *Geochimica et Cosmochimica Acta* 245, 577–596. https://doi.org/10.1016/j.gca.2018.10.004

Schiller, M., Bizzarro, M., Siebert, J. (2020) Iron isotope evidence for very rapid accretion and differentiation of the proto-Earth. *Science Advances* 6, 1–7. https://doi.org/10.1126/sciadv.aay7604

Tang, H., Dauphas, N. (2012) Abundance, distribution, and origin of 60Fe in the solar protoplanetary disk. *Earth and Planetary Science Letters* 359–360, 248–263. https://doi.org/10.1016/j.epsl.2012.10.011

Weyer, S., Schwieters, J.B. (2003) High precision Fe isotope measurements with high mass resolution MC-ICPMS. *International Journal of Mass Spectrometry* 226, 355–368. https://doi.org/10.1016/S1387-3806(03)00078-2

Weyrauch, M., Zipfel, J., Weyer, S. (2021) The relationship of CH, CB, and CR chondrites: Constraints from trace elements and Fe-Ni isotope systematics in metal. *Geochimica et Cosmochimica Acta* 308, 291–309. https://doi.org/10.1016/j.gca.2021.06.009

Williams, C.D., Sanborn, M.E., Defouilloy, C., Yin, Q.Z., Kita, N.T., Ebel, D.S., Yamakawa, A., Yamashita, K. (2020) Chondrules reveal large-scale outward transport of inner Solar System materials

in the protoplanetary disk. *Proceedings of the National Academy of Sciences of the United States of America* 117, 23426–23435. https://doi.org/10.1073/pnas.2005235117

Wölfer, E., Budde, G., Kleine, T. (2023) Age and genetic relationships among CB, CH and CR chondrites. *Geochimica et Cosmochimica Acta* 361, 288–301. https://doi.org/10.1016/j.gca.2023.10.010

Yokoyama, T., Nagashima, K., Nakai, I., Young, E.D., Abe, Y., *et al.* (2022) Samples returned from the asteroid Ryugu are similar to Ivuna-type carbonaceous meteorites. *Science* 379, 2003–2005. https://doi.org/10.1126/science.abn7850